Available online at www.sciencedirect.com

jmr&t Journal of Materials Research and Technology

journal homepage: www.elsevier.com/locate/jmrt

Original Article

Refining microstructure of medium-thick AA2219 aluminium alloy welded joint by ultrasonic frequency double-pulsed arc

Yipeng Wang [a], Hong Li [a], Zhuoxin Li [a], Yu Zhang [a], Jian Qin [b], Guangyu Chen [b], Bojin Qi [c], Caiyou Zeng [c,**], Baoqiang Cong [c,*]

[a] Department of Materials Science and Engineering, Faculty of Materials and Manufacturing, Beijing University of Technology, Beijing, 100124, China

[b] Welding Engineering and Laser Processing Centre, Cranfield University, Cranfield, United Kingdom

[c] School of Mechanical Engineering and Automation, Beihang University, Beijing, 100191, China

ARTICLE INFO

Article history:
Received 9 December 2022
Accepted 24 January 2023
Available online 29 January 2023

Keywords:
Aluminum alloy
Double pulse
Tungsten inert gas welding
Microstructure
Mechanical property

ABSTRACT

The increasing demand for achieving high-efficiency and high-quality medium-thick aluminium alloy welded structures, especially for large scale aerospace components, presents an urgent challenge to the conventional TIG arc welding process. This work proposed a novel double-pulsed variable polarity tungsten inert gas (DP-VPTIG) arc, in which the variable polarity square wave current was simultaneously modulated into ultrasonic frequency (20–80 kHz) and low frequency (0.5–10 Hz) pulses. Full penetration welds of 6 mm thick AA2219 aluminum alloy were successfully obtained by using this process. The microstructure and mechanical properties of the weld produced by DP-VPTIG arc were investigated, taking the conventional VPTIG arc as a comparative study. Results show that the microstructure of weld zone by DP-VPTIG arc showed an alternating distribution of fine equiaxed grain band and slightly coarse equiaxed grain band. Compared to VPTIG arc, the grain structure was effectively refined in the weld zone with DP-VPTIG arc, showing a significant reduction of average grain size by 51.2% along transverse section and 61.3% along longitudinal section. The morphology of α-Al+θ-$CuAl_2$ eutectics transformed from continuously distributed netlike shape to separately distributed granular shape, and segregation of Cu solute element was obviously improved. The average microhardness of weld zone was increased by about 8.7% and 5.6% along transverse section and along longitudinal section. The tensile properties of ultimate tensile strength, yield strength and elongation were increased by 6.6%, 10.6% and 20.5%, respectively. The results provide a valuable basis for improving welding efficiency and joint quality through a hybrid pulsed arc.

* Corresponding author.
** Corresponding author.
E-mail addresses: zengcy@buaa.edu.cn (C. Zeng), congbq@buaa.edu.cn (B. Cong).

https://doi.org/10.1016/j.jmrt.2023.01.174

1. Introduction

As an important structural material, AA2219 Al-6.3Cu (wt.%) aluminium alloy has been extensively applied in the aerospace industry, due to its excellent specific strength, fracture toughness and stress corrosion resistance [1]. As so far, with considerable process adaptability and economic benefits, variable polarity tungsten inert gas (VPTIG) welding is one of the most commonly used technologies for joining and fabrication of AA2219 aluminium alloy aerospace structures [2].

Limited by the free burning of TIG arc and the consequent low energy density, the penetration capability of VPTIG process is relatively low in comparison to other arc welding processes such as metal inert gas (MIG) welding and plasma arc welding (PAW), which makes this process particularly suitable for thin sheet ($\leq$3 mm) welding [3]. In terms of joining of medium-thick plates (5–8 mm), multi-layer multi-pass or high current levels welding is usually required. The former will largely increase the process complexity and reduce production efficiency, while the latter will bring about a significant increase in heat input, inducing coarse grain structures in the weld zone and a reduction in joint mechanical properties. Moreover, due to the high thermal conductivity of aluminium alloy, the heat obtained from the diverging arc heat source is easily conducted away, resulting in a large weld pool in the case of high heat input welding [4]. This deteriorates the process stability as the tendency of weld pool to collapse under the force of gravity is aggravated. These shortcomings of VPTIG welding process limit its application in the welding of medium-thick aluminium alloys. How to improve welding efficiency under the premise of ensuring good joint quality is a thorny challenge for the application of VPTIG process to aluminium alloy plates.

To overcome these obstacles and to meet the growing demand for high efficiency and high quality TIG welded structures of aluminium alloy plates, a great deal of effort has been made over these years. Activated TIG, referred as A-TIG, is a process in which the activating flux (halides or oxides) is smeared on the surface of the base metal prior to welding [5]. In this process, weld penetration as well as the ratio of weld depth to width can be distinctly enhanced because the surface tension induced Marangoni convection inside the weld pool changes from outward to inward [6]. Meanwhile, the weld shape of different regions can be controlled separately by applying different types and amounts of activating fluxes to the targeted areas [7]. However, the additional smearing process affects its production efficiency and it is difficult to guarantee uniform spreading of the activating flux especially for the complex structures. In addition, mixed shielding gases have been introduced to promote weld penetration by altering the arc characteristics and weld pool fluid flow. Traidia et al. and Xiang et al. investigated the effects of argon-helium mixtures on arc properties and weld geometry via different transient arc and weld pool models [8,9]. Results revealed that with the addition of helium to argon shielding gas, the arc temperature, the heat flux and current density as well as the weld penetration were considerably increased. Lu et al. developed a double-shielded TIG process using Ar + CO_2 mixed gases as the outer shielding layer and CO_2 gas as the inner shielding layer for welding SUS304 stainless steel [10]. It indicated that the inert argon gas in the inner layer can effectively prevent the gas in the outer layer from oxidizing the tungsten electrode, and the gas in the outer layer, which played a similar role as the activating flux for the weld pool, can obviously improve the welding efficiency. The composition of the inner layer gas and the outer layer gas can be flexibly adjusted when this process is used for different base metals [11]. Additionally, the assistance of external energy fields such as longitudinal magnetic field [12], ultrasound field [13] and their hybrid [14] have been proved to be effective in enhancing weld penetration and production efficiency. The disadvantage of these methods is that they require auxiliary external energy field generating devices and fixtures attached to the motion system, which not only increases the equipment cost and process complexity, but also reduces process adaptability.

Pulse modulation (low-frequency pulse, high-frequency pulse) of welding current waveform is considered to be one of the most promising technologies for the improvement of TIG welding process. Wang et al. indicated that high-frequency pulses (normally above 5 kHz) can induce notable arc constriction and increase arc stiffness as well as energy density [15]. Yang et al. experimentally measured the arc force and demonstrated that by pulsing the arc at ultrasonic frequency (over 20 kHz), the average arc force was increased by 42–57% compared to conventional welding arc [16]. Onuki et al. compared the differences between ultrasonic frequency pulsed arc and non-pulsed arc with an equal average power input [17]. They identified that the arc pressure and weld depth were 3 times as high and twice as deep as those obtained by non-pulsed arc. Low-frequency pulses (typically less than 10 Hz) have also been introduced in the arc welding process. It was found that by flexibly adjuting pulse parameters, the low-frequency pulsed arc can visibly stabilize the weld pool and widen the current window when implementing high penetration TIG welding [18]. The grain structure can be refined by the stirring effect of the low-frequency pulsed arc through breaking the dendrites during solidification [19].

Inspired by above-mentioned works, with the purpose to further improve the TIG process by taking full advantage of ultrasonic frequency pulse and low-frequency pulse, a DP-VPTIG process was proposed, in which the variable polarity square wave current was innovatively modulated into ultrasonic frequency (20–80 kHz) and low-frequency (0.5–10 Hz) pulses. Our preliminary work has revealed the process characteristics of DP-VPTIG including the evolution of arc profile and weld pool geometry, the microstructural characterization and tensile properties of 4 mm thick AA2219 aluminium alloy welded joints [20]. Based on this, through optimal current parameters combination, a stable “one-pulse one-keyhole” mode full penetration high efficiency welding of 7 mm thick AA2219 aluminium alloy has been successfully achieved, and the mechanism of weld pool surface and keyhole evolution under the effect of double-pulsed arc has been illuminated [21]. However, the microstructure and mechanical properties of medium-thick AA2219 aluminium alloy welded joints produced by DP-VPTIG process has not been fully understood. The aim of this work is to investigate the effects of ultrasonic frequency double-pulsed arc on the microstructure evolution and mechanical properties of medium-thick AA2219

aluminium alloy welded joints. The results will lay a solid foundation for a better understanding of DP-VPTIG welding process, which may provide a new approach to simultaneously improve welding efficiency and joint quality of medium-thick aluminium alloy welded structures.

2. Experimental procedure

AA 2219-T87 aluminium alloy plates (6 mm thick) were employed as the base metal, whose chemical composition is Cu 6.3%, Mn 0.28%, Ti 0.1%, Zr 0.19%, Fe 0.2%, Si 0.17%, Al balance (all in mass fraction). T87 represents that the material had sequentially experienced solution heat treatment, cold working by 7% stretching and artificial aging treatment. The microstructure of the base metal is shown in Fig. 1. It can be clearly observed that the grain structure as well as the second phase had been elongated along the rolling direction, presenting a thin and long morphological feature. The gauge dimension of the work-pieces for welding was 200 mm × 100 mm × 6 mm. The shielding gas adopted was 99.99% pure argon. No filler material was used.

A self-developed DP-VPTIG welding power supply was applied for the investigation, whose current waveform is illustrated in Fig. 2. From the figure, the variable polarity square wave current was simultaneously modulated into ultrasonic frequency (20–80 kHz) and low frequency (0.5–10 Hz) pulses. The feature current parameters of the DP-VPTIG process include variable polarity square wave frequency ($f_v = 1/T_v$), duration of positive phase (t_{vp}), duration of negative phase (t_{vn}); ultrasonic-pulsed frequency (f_{UP}), duty cycle of ultrasonic frequency pulse (δ_{UP}), ultrasonic frequency pulse value (I_{UP}); low-pulsed frequency ($f_L = 1/T_L$), duration of low-frequency pulse peak phase (t_p), duration of low-frequency pulse base phase (t_b), duty cycle of low-frequency pulse (δ_L), positive current during t_p (I_{pp}), negative current during t_p (I_{pn}), positive current during t_b (I_{bp}), negative current during t_b (I_{bn}). Limited by the design of the power supply, all pulse current parameters can be set separately except for I_{pn} and I_{bn}, which means that I_{pn} and I_{bn} must be equal to I_{pp} and I_{bp}, respectively ($I_{pn} = -I_{pp}$, $I_{bn} = -I_{bp}$).

Single pass butt welding experiments were carried out to achieve full penetration welds by conventional VPTIG, served as a comparative study, and DP-VPTIG processes. According to preliminary parametric tests and research results [19,20,22], the optimal combination of ultrasonic-pulsed frequency of 20 kHz and low-pulsed frequency of 2 Hz were selected for the study. Other current parameters of DP-VPTIG were f_v 100 Hz, t_{vp}:t_{vn} 4:1; δ_{UP} 50%, I_{UP} 80 A; δ_L 50%, I_{pp}/I_{pn} 350/-350 A, I_{bp}/I_{pn} 180/-180 A. The current parameters of conventional VPTIG were $f_{v'}$ 100 Hz, $t_{vp'}$:$t_{vn'}$ 4:1, $I_{p'}$/$I_{n'}$ 297/-297 A. The average current values of both arc modes were substantially the same to avoid the effect of differences in heat input on the results. The shielding gas flow rate was 15 L min^{-1}, the electrode (cerium-tungsten) diameter was 4 mm, and the welding speed was 170 mm min^{-1}.

Prior to welding, all the work pieces were mechanically ground and cleaned with acetone to remove surface contamination. Fig. 3a schematically illustrates the position of specimens used for microscopic observation and mechanical properties testing. All specimens were taken from the middle part of the welds. Metallographic samples were sequentially ground, polished and etched in the Keller's reagent solution with a chemical composition of HNO_3 2.5%, HCL 1.5%, HF 1% and H_2O 95% (all in volume fraction). Microstructure feature was investigated by using AX10 typed optical microscope (OM) as well as ZEISS EVO-18 typed scanning electron microscope (SEM). Elemental analysis was conducted with energy dispersive spectrometry (EDS), which was equipped with SEM. The HVD-1000TEST typed digital Vickers (HV) hardness tester was employed for microhardness testing, and the loading force was set to 1.96 N with a duration of 15 s. As shown in Fig. 3b, the microscopic observation and microhardness testing were respectively carried out along the longitudinal section and transverse section. All specimens for tensile testing were machined based on standard metallographic procedures, as presented in Fig. 3c. The DWD-50E typed electronic universal testing machine was used for tensile testing, and it was conducted at ambient temperature with a loading rate of 2 mm/min.

3. Results

3.1. Grain morphology of weld zone

Representative macrographs of the weld zone along the transverse section with VPTIG arc and DP-VPTIG arc are

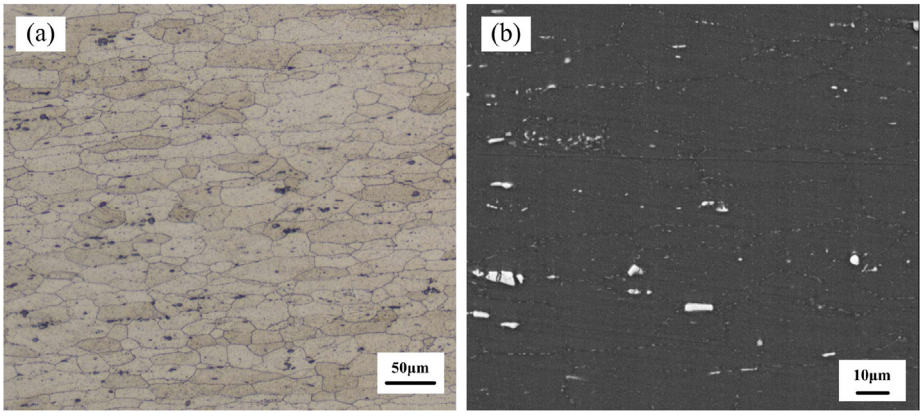

Fig. 1 – Microstructure of AA2219-T87 aluminium alloy plate. (a): OM image; (b): SEM backscattered electron image.

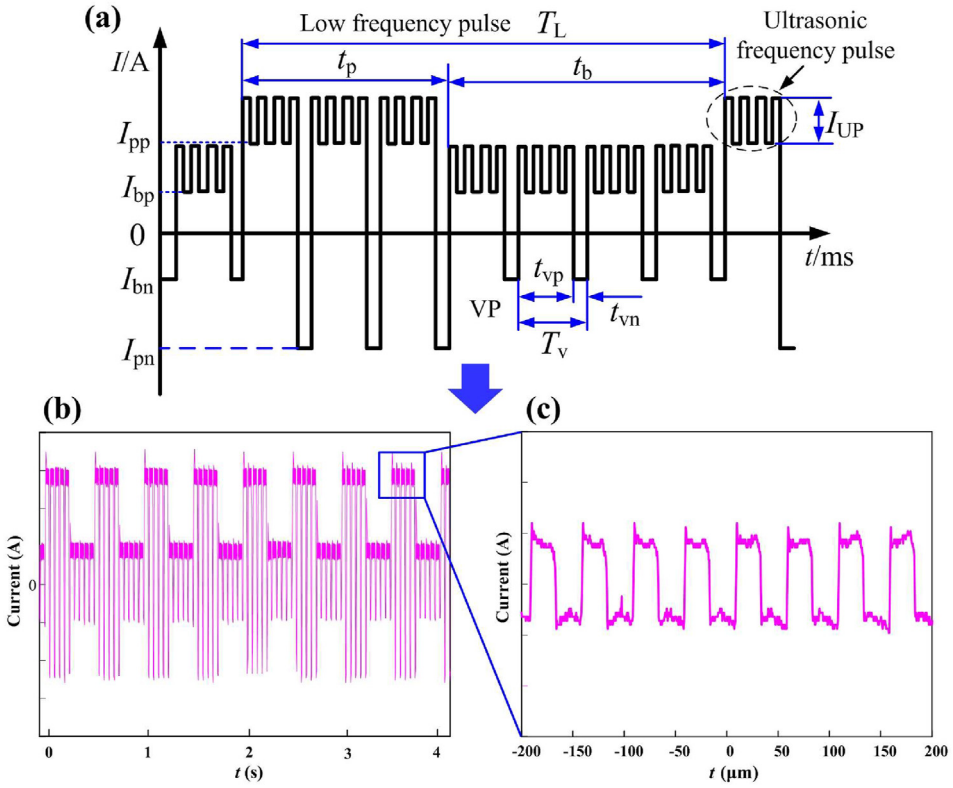

Fig. 2 – Current waveform of DP-VPTIG process. (a): Schematic diagram; (b): Actual waveform; (c): Ultrasonic frequency pulses (20 kHz).

shown in Fig. 4. The VPTIG weld zone exhibited a typical dendritic microstructure, which was comprised of coarse columnar and equiaxed dendrites. A large number of eutectic phases existed between the dendrite arms, as shown in the enlarged view of Fig. 4c. In contrast, the microstructure of DP-VPTIG weld zone was refined significantly, consisting of fine equiaxed and columnar grains. The enlarged view (Fig. 4f) indicated those refined α-Al grains were without dendrite growth characteristics. Observable porosity defects were not found in these two weld zones.

On the longitudinal sections, representative grain morphologies of the weld zone produced by conventional VPTIG

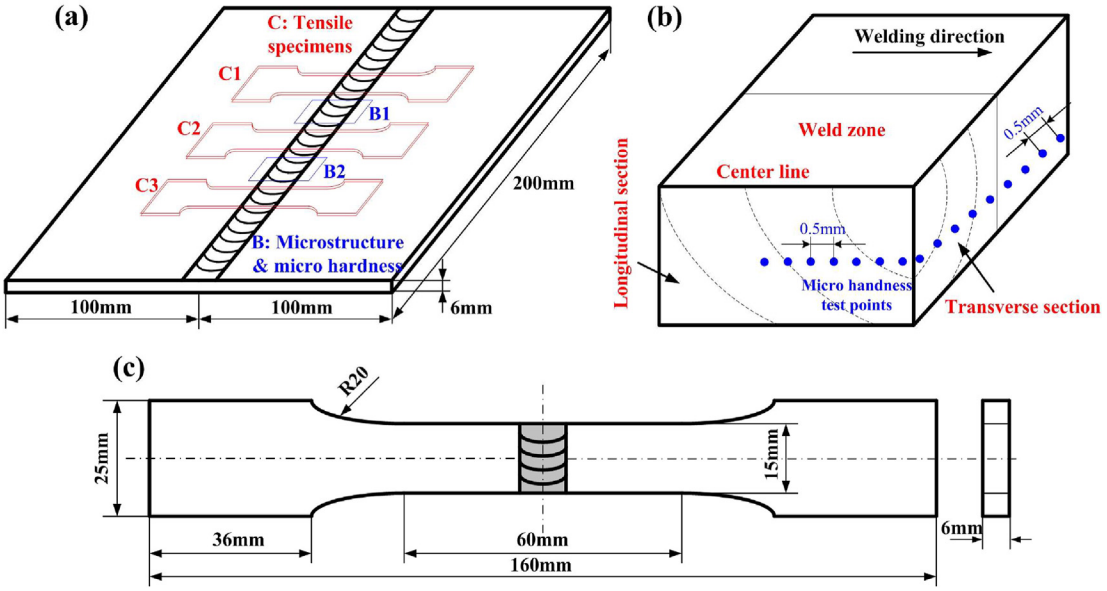

Fig. 3 – Schematic illustration of the specimens. (a): Position for testing; (b): Microstructure and microhardness test (c): Dimension of tensile specimens.

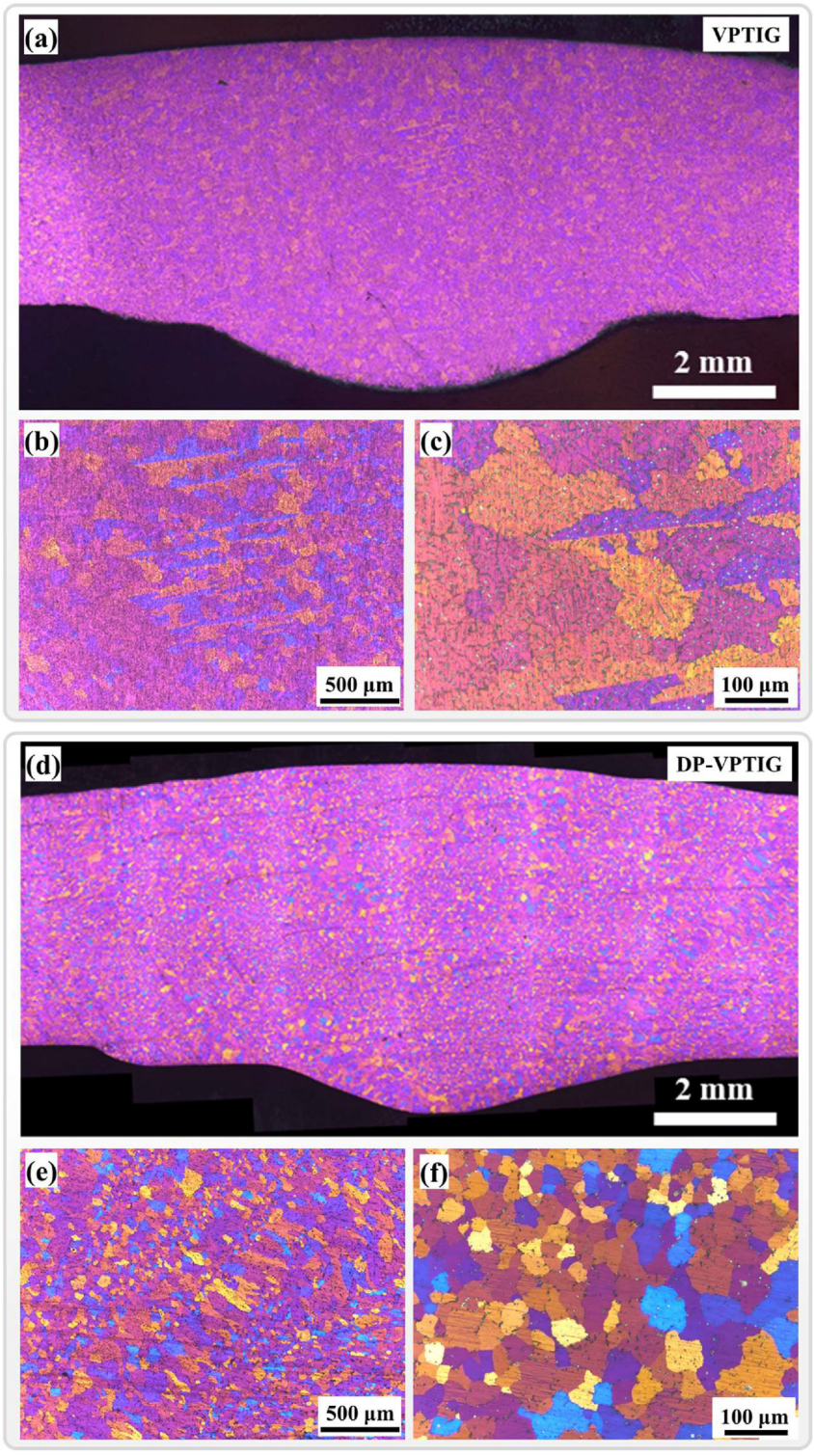

Fig. 4 – Montages and optical micrographs with different magnifications showing the typical microstructure along the transverse section. (a)–(c): Weld zone by VPTIG arc; (d)–(f): Weld zone by DP-VPTIG arc.

arc and DP-VPTIG arc are displayed in Fig. 5. From Fig. 5a–c, it can be clearly observed that the microstructure with VPTIG arc was mainly characterized by coarse columnar dendritic grains, which exhibited the same grain orientation along the welding direction as well as along the weld bottom to weld surface. Obvious segregation of the solute element can be recognized between the dendrites and on the surface of grains in the form of diffusely distributed particles. For DP-VPTIG process, the microstructure of weld zone presented a band-like distribution of fine equiaxed grain band (FEGB) and slightly coarse equiaxed grain band (CEGB), as shown in Fig. 5d–f. These two grain bands alternated regularly along

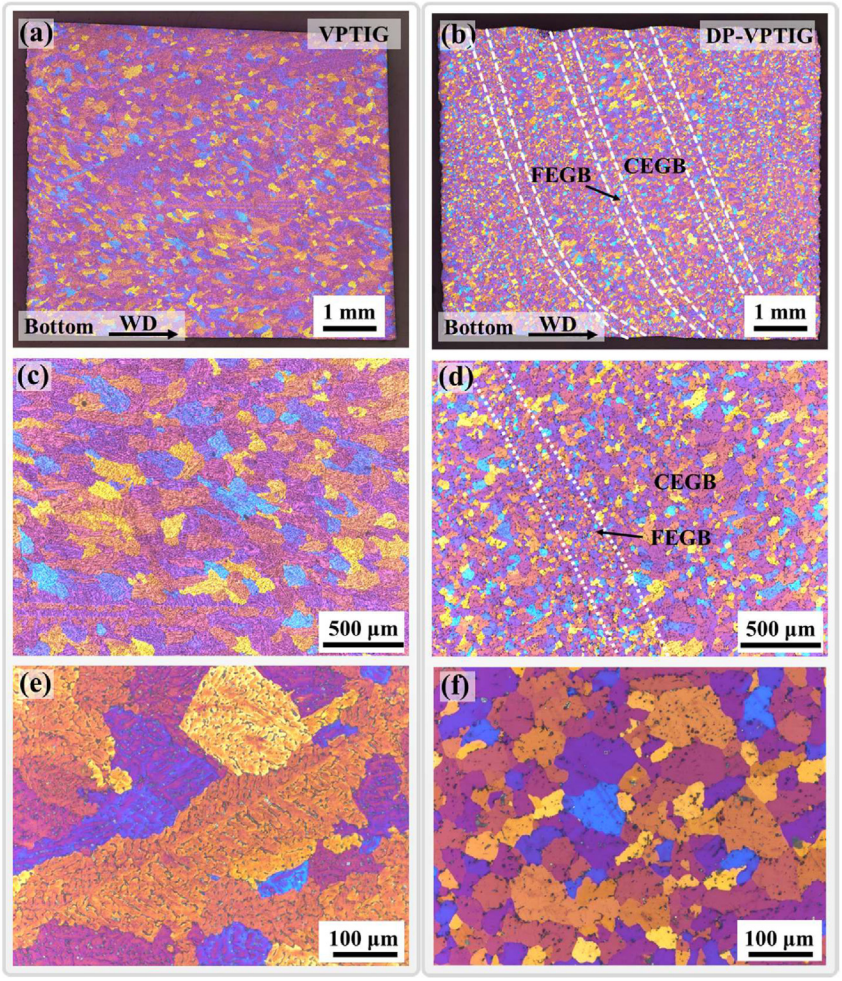

Fig. 5 – Optical micrographs of weld zone along longitudinal section. (a)–(c): Weld zone by VPTIG arc; (d)–(f): Weld zone by DP-VPTIG arc.

the welding direction, accompanied by high and low fluctuation of weld surface, which has been proved to be caused by low-frequency pulsed current as reported by our previous research on bead formation characteristics of DP-VPTIG arc [19].

The grain misorientation on the transverse and longitudinal sections of the weld zone produced by conventional VPTIG arc and DP-VPTIG arc is characterized by EBSD inverse pole figures mapping and pole figures, as shown in Fig. 6. Large-scale columnar dendrite grain domains with preferential orientations of <101> and <111> can be observed clearly from the inverse pole figure mapping of the transverse VPTIG weld zone. The maximum values of the multiples of uniform distribution (MUD) of the VPTIG weld zone along the transverse and longitudinal sections were 2.578 and 1.738, respectively. Comparatively, the maximum values of MUD of the transverse and longitudinal weld zones via DP-VPTIG arc were 1.519 and 1.614, and lower than those of the VPTIG weld zone. Obtained EBSD results indicate that the VPTIG weld zone possesses a stronger preferred orientation compared with the DP-VPTIG weld zone.

EBSD grain size mappings and statistical distribution of grain size with VPTIG arc and DP-VPTIG arc are provided in Fig. 7. The weld zone with VPTIG arc exhibited a relatively uniform grain size distribution along the transverse and longitudinal sections, corresponding to the uniform distributed blue and green color, respectively. EBSD grain size mappings of the DP-VPTIG weld zone indicated a distinct band-like distribution alternating with FEGB and CEGB along transverse and longitudinal sections, which is consistent with the optical metallographic results of Figs. 4 and 5. From the quantitative statistical results of grain size, it reveals that the average grain diameter of the weld zone with VPTIG arc was 109.9 μm along the transverse section and 136.3 μm along the longitudinal section. Additionally, the area fraction of grains smaller than 50 μm was 23.9% and 6.5%, respectively. Comparely, the grain structure was remarkably refined by DP-VPTIG arc, whose average grain size of weld zone was decreased by around 51.2% and 61.3% in comparison to that of VPTIG arc along the transverse and longitudinal sections. In addition, the area fraction of grains with a diameter less than 50 μm reached up to 59.7% and 55.6% with DP-VPTIG arc along the transverse and longitudinal sections.

The grain boundary characteristics of the VPTIG and DP-VPTIG weld zones were investigated by EBSD and presented in Fig. 8. For the results of grain misorientation angle, its

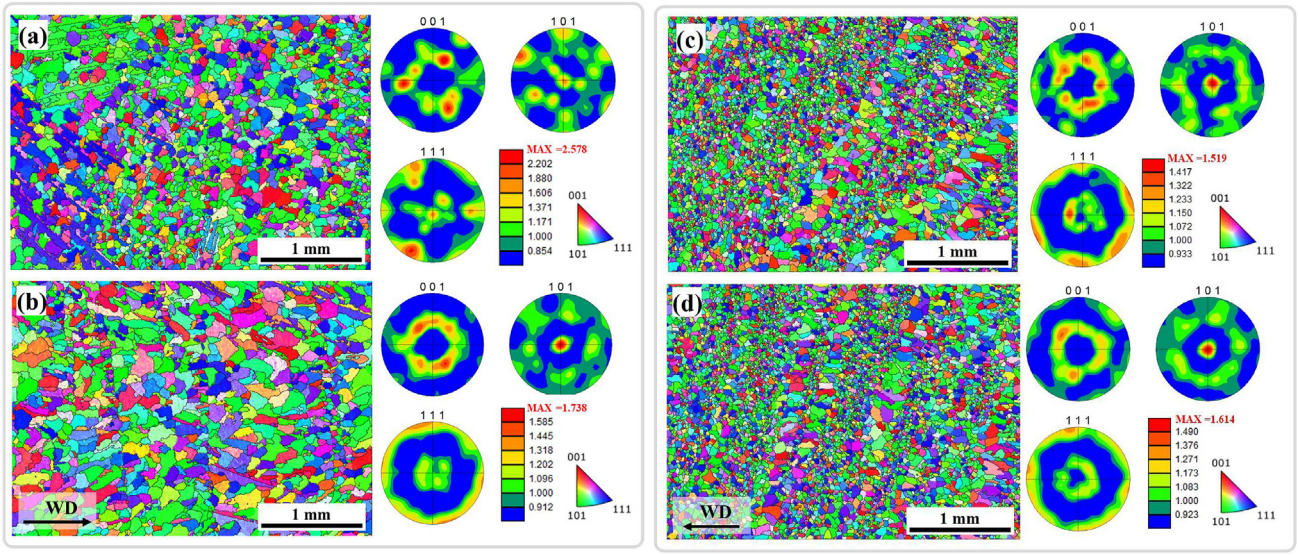

Fig. 6 – Inverse pole figures mapping and pole figures of weld zone. (a) and (b): Transverse and longitudinal section via VPTIG arc; (c) and (d): Transverse and longitudinal section via DP-VPTIG arc.

average value was respectively 21.7° and 16.7° with VPTIG arc along the transverse and longitudinal sections. The grain misorientation angle with DP-VPTIG arc increased remarkably compared with that of VPTIG arc. Both of the average values along the transverse and longitudinal sections reached up to 36.2°. In addition, the density of low angle grain boundary (LAGB) in the weld zone with DP-VPTIG arc was reduced prominently compared with the one with VPTIG arc. Thus, a high-density high angle grain boundary (HAGB) became dominant in the DP-VPTIG weld zone, as shown in Fig. 8c and d. From the statistical results, the number fraction of the LAGB was 54.4% and 64.1% with VPTIG arc along the transverse and longitudinal sections, but only 15.9% and 16.1% with DP-VPTIG arc along the corresponding sections. The high-density LAGB observed in the weld zone with VPTIG arc is closely related to the dendritic characteristics.

3.2. *Second phase in weld zone*

To figure out the second phase morphology and distribution of Cu solute element in the weld zone, SEM observation and EDS analysis were carried out. SEM micrographs of the weld zone showing the second phase morphology with VPTIG arc and DP-VPTIG arc are demonstrated in Fig. 9. Clearly, it can be seen in Fig. 9a and b that there were a great number of white netlike shape and coarse α-Al+θ-$CuAl_2$ eutectics continuously distributed at grain boundaries in the VPTIG weld. Also, numerous fine granular α-Al+θ-$CuAl_2$ eutectics and dispersive θ-$CuAl_2$ particles scattered on the grain surface can be detected. In contrast, there were much less continuously distributed netlike shape α-Al+θ-$CuAl_2$ eutectics but more separate granular θ-$CuAl_2$ particles existed in the weld zone with DP-VPTIG arc, which can be clearly observed in Fig. 9d and e. Besides, the area fraction of second phase was calculated by using binarized images (Fig. 9c and f) through counting the number ratio of pixel points with a gray value of 1 to the total number of pixel points. Results showed that the second phase area fraction of VPTIG weld was 6.2% and it decreased to 2.4% in DP-VPTIG weld, revealing that the number of α-Al+θ-$CuAl_2$ eutectic structures was greatly decreased and their sizes were all distinctly reduced.

Further analysis of the second phase, and the distribution of Al and Cu elements using EDS mapping and line scanning taking the marked areas in Fig. 9 are illustrated in Fig. 10. Typical eutectic phase with a mixture of α-Al and θ-$CuAl_2$ can be found obviously in the weld zone with VPTIG arc. While, a typical divorced eutectic phase, consisting only of θ-$CuAl_2$ phase, formed in the DP-VPTIG weld zone. From the EDS mapping results in Fig. 10a and c, serious enrichment of Cu element in the eutectic and divorced eutectic phase can be obviously recognized with both VPTIG arc and DP-VPTIG arc. Line scanning results revealing the detailed distribution curve of Al and Cu elements from α-Al matrix across the α-Al+θ-$CuAl_2$ eutectics are shown in Fig. 10b and d. From the curve, there was a steep drop in Cu concentration as it moved from the α-Al matrix to the eutectic structure. In Fig. 10b with conventional VPTIG arc, the α-Al matrix contained Al 98.4 at% and Cu 1.6 at%, and the eutectics contained Al 79.5 at % and Cu 20.5 at %, indicating that severe Cu solute element segregation existed in the weld zone. As for DP-VPTIG arc, the Al concentration was 97.3 at% and Cu concentration was 2.7 at% in the α-Al matrix, and they were 70.1 at% and 29.9 at%, respectively, in the eutectics. This suggested that the segregation of Cu element was significantly improved with DP-VPTIG arc compared with VPTIG arc.

3.3. *Microhardness*

Microhardness distribution of weld zone along the transverse section by VPTIG and DP-VPTIG processes is depicted in Fig. 11a. From the results, it can be found that the average microhardness was 69 HV with VPTIG arc, while it increased up to 75 HV with DP-VPTIG arc, which means that there is an increment of around 8.7% along the transverse section. Fig. 11b

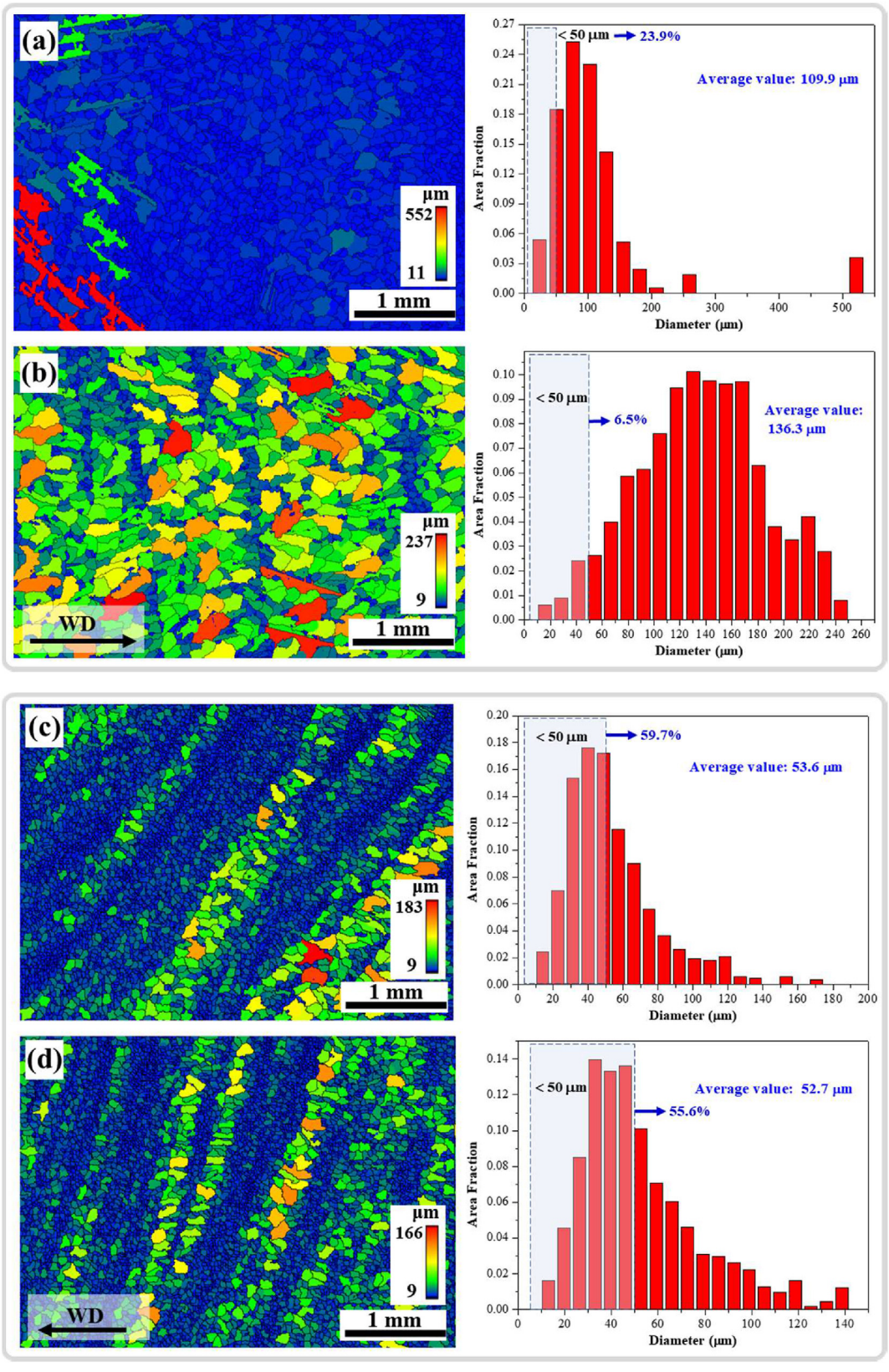

Fig. 7 – EBSD grain size mappings and the statistical grain size distribution of the weld zones. (a) and (b): Transverse and longitudinal section via VPTIG arc; (c) and (d): Transverse and longitudinal section via DP-VPTIG arc.

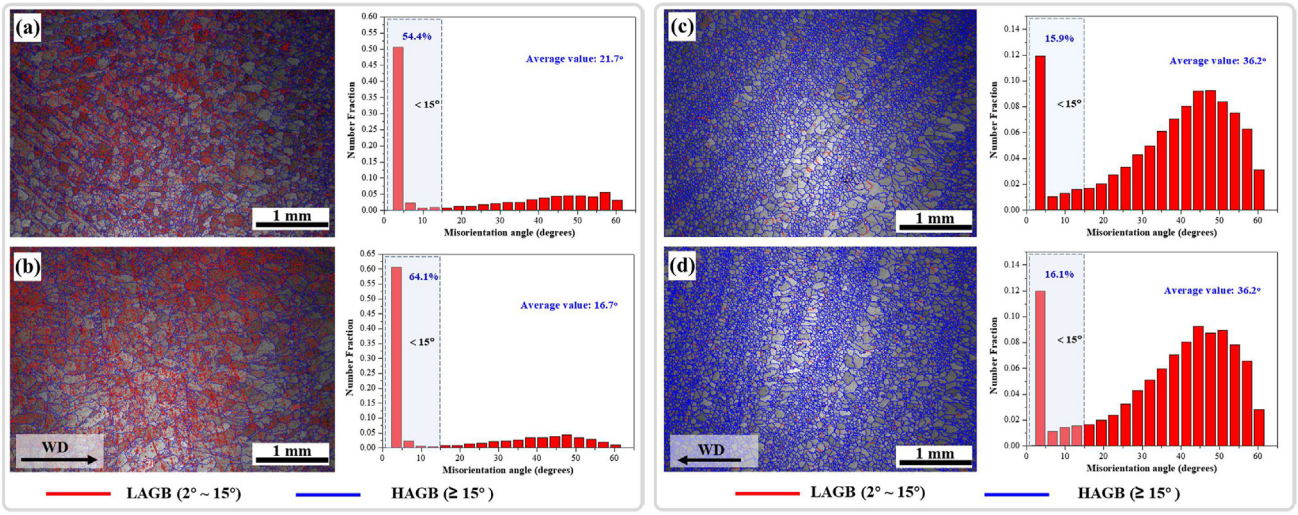

Fig. 8 – EBSD grain boundary mappings and the statistical misorientation angle distribution of the weld zones. (a) and (b): Transverse and longitudinal section via VPTIG arc; (c) and (d): Transverse and longitudinal section via DP-VPTIG arc.

shows the microhardness distribution of the weld zone along the longitudinal section. For the weld zone with VPTIG arc, microhardness values were distributed between 69 HV and 75 HV, and the variation range (6 HV) was comparatively wide. In comparison, the weld zone with DP-VPTIG arc showed an improvement in the uniformity of microhardness distribution, as its variation range decreased to 5 HV, ranging from 73 HV to 78 HV. The average microhardness of VPTIG and DP-VPTIG were 72 HV and 76 HV, respectively, suggesting there was an increment of around 5.6% in average microhardness of the weld zone along the longitudinal section by DP-VPTIG arc. Comparison results of average microhardness between transverse section and longitudinal direction indicate that the difference of these two directions with VPTIG arc is more significant than that of DP-VPTIG arc, reflecting better isotropy of mechanical property can be achieved by DP-VPTIG arc.

3.4. *Tensile properties*

Fig. 12 displays the tensile properties, involving the ultimate tensile strength (UTS), yield strength (YS) and elongation, of the joints fabricated by VPTIG and DP-VPTIG processes. All the fractures occurred in the weld zone. Compared with the tensile properties of base metal (UTS 458 MPa, YS 251 MPa and elongation 12.3%), the joints of both VPTIG arc and DP-VPTIG arc showed significant reductions in all three indicators. This is mainly because of the solidification microstructure formed in the weld zone. As described in Section 2, AA2219-

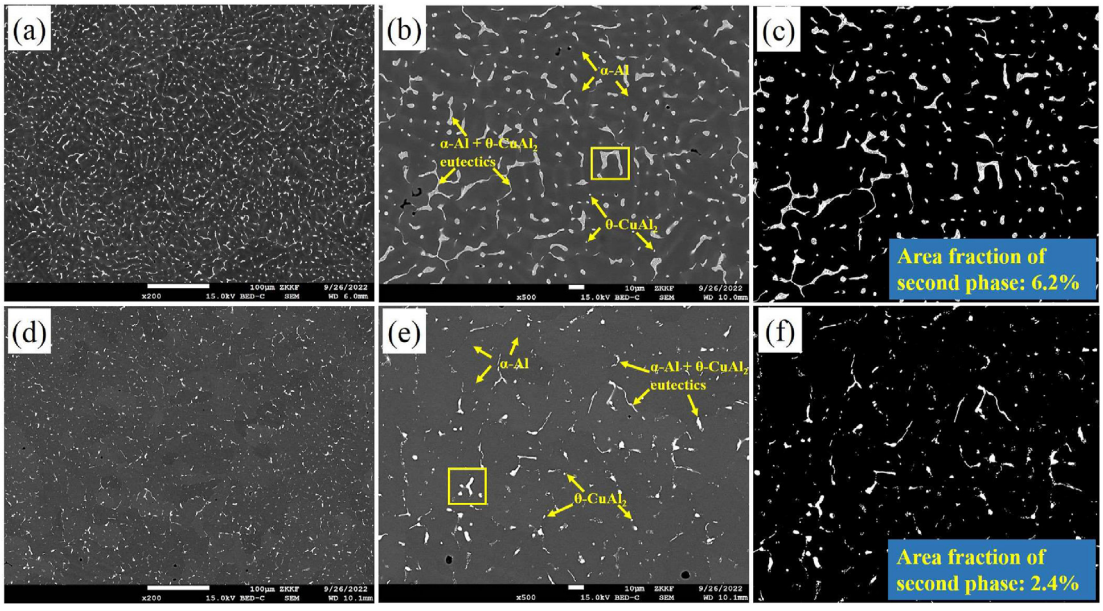

Fig. 9 – SEM backscattered electron micrographs of weld zone. (a): ×200 VPTIG; (b) and (c): ×500 VPTIG and its binarized image; (d): ×200 DP-VPTIG; (e) and (f): ×500 DP-VPTIG and its binarized image.

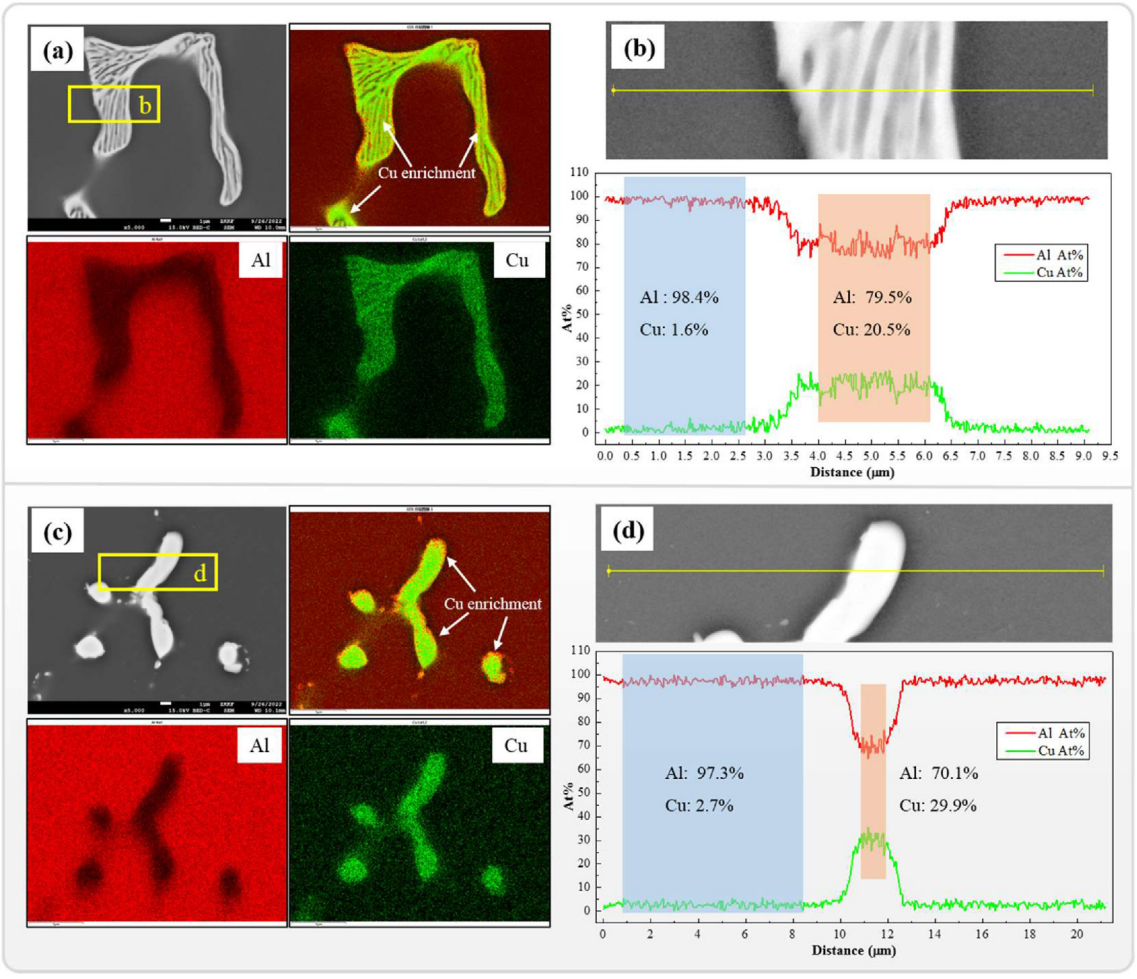

Fig. 10 – EDS mapping and line scanning results of Al and Cu in the weld zone. (a): EDS mapping, VPTIG; (b): Line scanning, VPTIG; (c): EDS mapping DP-VPTIG; (d): Line scanning VPTIG.

T87 aluminium alloy is a working hardened and heat treatment strengthened material. After the process of melting and solidification, the original hardening effect completely disappeared. Meanwhile, the segregation of Cu alloying element in the weld zone significantly decreased the solution and precipitation strengthening effects. UTS, YS and elongation of the joints with VPTIG arc were 256 MPa, 141 MPa and 4.4%, respectively. The joints with DP-VPTIG arc presented a UTS of 273 MPa, YS of 156 MPa and elongation of 5.3%, which exhibits an increment of 6.6%, 10.6% and 20.5%, respectively, compared to those of VPTIG arc.

Fig. 13 demonstrates SEM micrographs of fracture morphologies for the specimens created by conventional VPTIG and DP-VPTIG processes, respectively. In the fractography

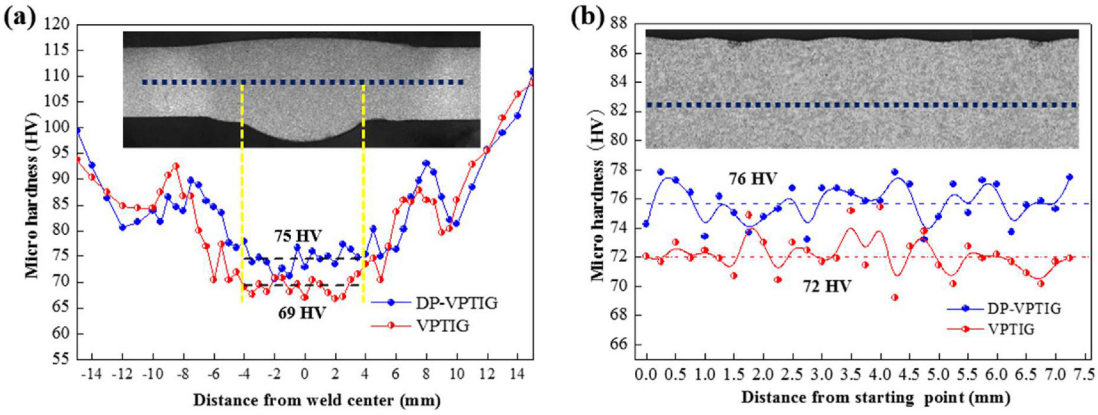

Fig. 11 – Microhardness distribution of weld zone. (a): Longitudinal section; (b): Transverse section.

with VPTIG arc, cleavage steps and dimples can be observed on the surface of the fracture, indicating mixed fracture characteristics of brittle and ductile. Analysed by EDS, the small particles at the bottom of the dimples are θ phase (point G: Al 69.81 at% and Cu 30.19 at%), and the large fractured phases were eutectics (point H: Al 85.39 at% and Cu 14.61 at%, point I: Al 89.12 at% and Cu 10.88 at%). Secondary cracks and micro-voids can also be found on the fracture surface, which may become the fracture source under static load. In the fractography with DP-VPTIG arc, there were plenty of dimples and tearing ridges uniformly distributed on the surface of the fracture, showing typical ductile fracture characteristics.

4. Discussion

4.1. *Mechanism of microstructure refinement*

According to the classical solidification principle, grain morphology is principally determined by the thermal gradient (*G*) and cooling rate (*R*) at the front of solid-liquid interface during solidification process. Higher *G* and slower *R* tend to form a columnar grain structure, while lower *G* and faster *R* contribute to the formation of an equiaxed grain structure [23]. In this study, with the purpose of achieving the fully penetrated single-pass weld of 6 mm thick AA2219 aluminum alloy, a high current level is inevitably applied to the conventional free diverging VPTIG arc. Consequently, excessive heat input brings about a high tendency of coarse columnar structures in the weld zone, due to the high thermal gradient and slow cooling rate at the front of solid-liquid interface. By introducing DP-VPTIG arc, the conventional variable polarity current waveform is simultaneously modulated into low frequency pulses and ultrasonic frequency pulses. Their combined effect not only significantly affects bead geometry by adjusting the characteristics of arc profile [20], but also changes the molten pool flow and the thermal history of the weld zone as discussed below.

On the one hand, regarding the effect of low frequency pulsing of arc, the arc profile as well as arc energy vary cyclically between high and low, accompanied by the pulse peak and pulse base current, as illustrated in Fig. 14. During the low frequency pulse peak stage (t_p), the transient arc profile is expanded and the arc energy is relatively high on account of the high current value (Fig. 14a). This leads to a higher thermal gradient (*G*) and a slower cooling rate (*R*) at the solid-liquid interface, which corresponds to the formation of CEGB in the DP-VPTIG weld zone. In low frequency pulse base stage (t_b), there is a dramatic reduction in the transient arc profile and arc energy attributed to the deep drop in the current value (Fig. 14b). As a result, the thermal gradient (*G*) at the solid-liquid interface is reduced and its cooling rate (*R*) is accelerated to a large extent, inducing the formation of FEDB in the weld zone. The spatially close correspondence between the band-like distribution of grain structure and the high and low fluctuation of the weld surface shown in Fig. 5 can verify this clarification. Compared with conventional VPTIG process, the generation of FEGB and FCGB via DP-VPTIG arc prominently interrupts the continuous growth of grains, which is considered to be an important mechanism for the refinement of grain structure by DP-VPTIG arc.

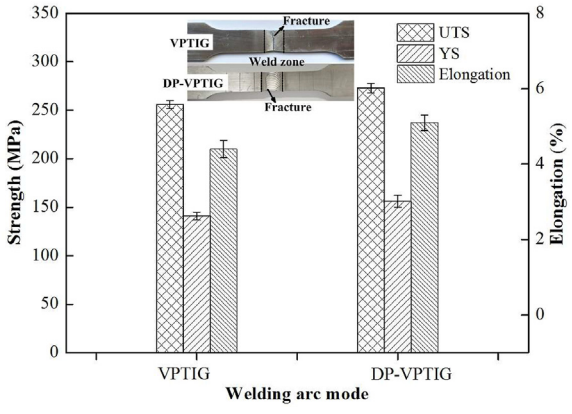

Fig. 12 – Tensile properties of joints by VPTIG arc and DP-VPTIG arc.

On the other hand, the periodical variation of the arc force along with the low frequency pulse simulates a "one-pulse one-keyhole" flow mode in the molten pool, as stated by [21]. In t_p, the arc force acting on the molten pool is relatively strong, resulting in a deep depression on the surface of molten pool (Fig. 14a). The opening of keyhole pushes the liquid metal away from the center of molten pool to its rear and side. As the current switches to t_b, the depression of molten pool surface is considerably weakened because of the significant reduction in arc force (Fig. 14b). In this stage, the liquid metal flows back from the rear and side of molten pool and refills the keyhole. By this unique "one-pulse one-keyhole" flow mode, the molten pool fluidity is greatly facilitated. With respect to ultrasonic frequency pulsing of arc, a great deal of research work have proved that the arc profile is substantially contracted and the arc stiffness is notably increased when ultrasonic frequency pulsed current is employed. Yang et al. investigated the surface depression of molten pool under the effect of ultrasonic frequency pulsed arc, and identified that double circulation flow can be created in the molten pool, which undoubtedly promotes the fluidity of molten pool [24]. Yuan et al. suggested that ultrasonic waves generated by the high frequency pulsing arc can cause cavitation and acoustic streaming in the molten pool, which will further enhance the vibration and fluidity of molten pool [25]. With the combination stirring effect of the abovementioned low frequency pulsing and ultrasonic frequency pulsing of arc, the fluidity of molten pool is greatly promoted. In this case, the existing dendrites at the rear of molten pool might be broken into small particles, and their fragmentations can serve as the nucleation sites grow into fine equiaxed grains, as schematically illustrated in Fig. 14. This phenomenon has already been experimentally observed by Yuan et al. [26], where the stirring effect of molten pool was provoked by transverse arc oscillation. The promotion of dendrite fragmentation is considered to be another mechanism for the refinement of grain structure by DP-VPTIG arc.

4.2. *Strengthening mechanism*

The improvement of microhardness and tensile properties with DP-VPTIG arc can be explained by the refinement of grain structure and the reduction in segregation of Cu alloying

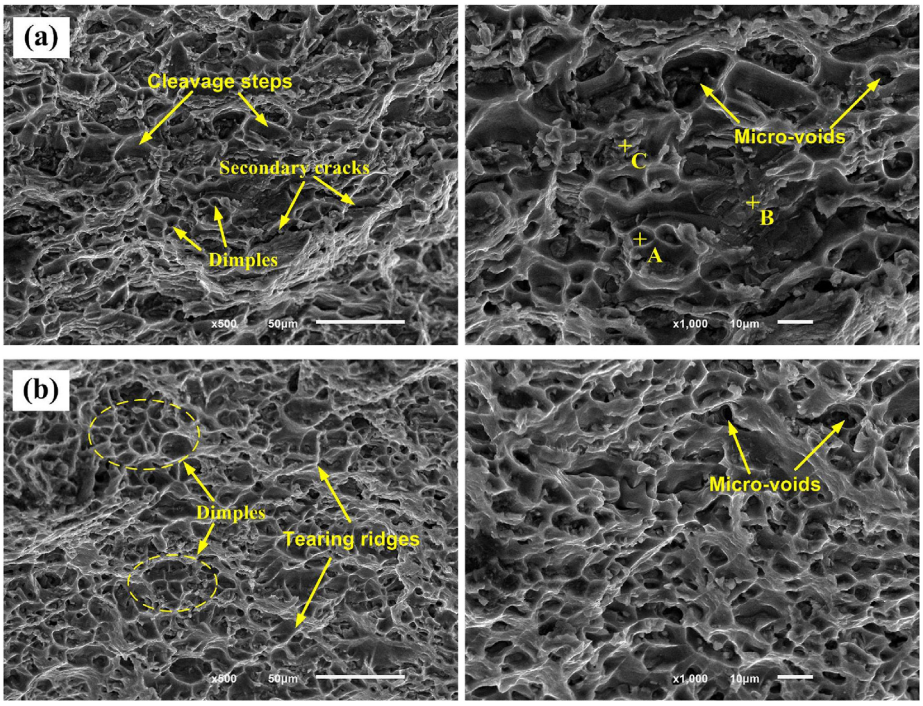

Fig. 13 – SEM secondary electron images of fracture morphology. (a): VPTIG arc; (b): DP-VPTIG arc.

element in the weld zone. On the one hand, it is well-known that the grain boundary plays an important role in hindering the motion of dislocation, thus enhancing the strength of the material. Refinement of the grain structure is able to effectively increase the density of grain boundaries, especially HAGBs, and further enhance the deformation resistance and reduce the stress concentration via increasing the uniformity of grain deformation [27]. On the other hand, solid solution strengthening and precipitation strengthening are another two crucial factors for the deformation behavior of AA2219 aluminium alloy. Severe segregation of Cu solute element can significantly reduce the amount of solid solution in α-Al

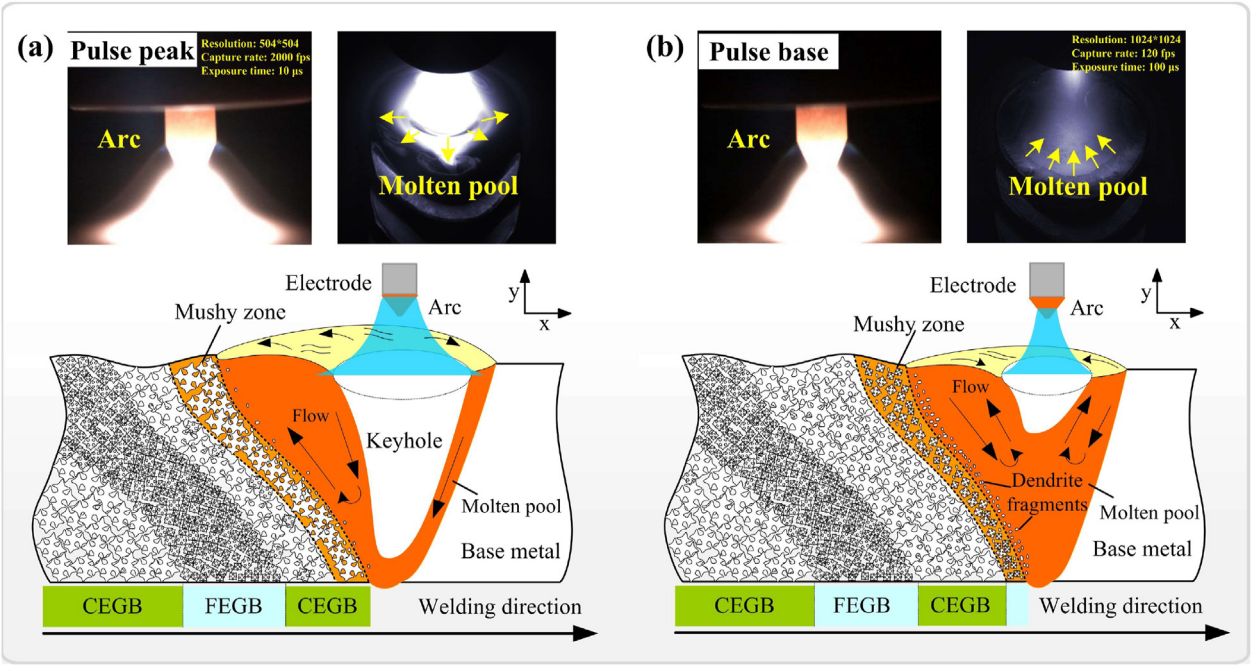

Fig. 14 – Mechanism of microstructure evolution by DP-VPTIG arc. (a): Low frequency pulse peak stage; (b): Low frequency pulse base stage.

matrix, bringing about a reduction in solid solution strengthening effect [28]. Furthermore, the existence of large and continuous α-Al+θ-$CuAl_2$ eutectics induces a high tendency of stress concentration and brittleness, which is detrimental to uniform plastic deformation and reduces elongation [29]. The obtained microstructural characterization results provide evidence that the DP-VPTIG arc can effectively inhibit the formation of coarse eutectic structures. Therefore, the DP-VPTIG arc can improve the uniform deformation capacity and strength. In a word, the DP-VPTIG arc provides a promising approach to simultaneously improve the microstructure of weld zone and mechanical properties of welded joints, especially for the high efficiency welding of medium thickness aluminium alloys.

5. Conclusions

In the present study, an evaluation of microstructure and mechanical properties of medium-thick AA2219 aluminium alloy weld produced by DP-VPTIG arc was carried out. The conventional VPTIG arc was employed as a comparative investigation. The main conclusions can be drawn as follows.

(1) Microstructure of weld zone by DP-VPTIG arc presented an alternating distribution of fine equiaxed grain band (FEGB) and slightly coarse equiaxed grain band (CEGB). Compared to VPTIG arc, the grain structure was effectively refined in the weld zone of DP-VPTIG arc, showing a significant reduction in average grain size by 51.2% along the transverse section and 61.3% along the longitudinal section.
(2) The morphology of α-Al+θ-$CuAl_2$ eutectics transformed from continuously distributed netlike shape by VPTIG arc to separately distributed granular shape by DP-VPTIG arc, and the number of eutectics decreased significantly in the weld zone. Also, the segregation of Cu solute element was obviously improved by DP-VPTIG arc.
(3) Compared to VPTIG arc, the average microhardness of weld zone by DP-VPTIG arc was increased by about 8.7% and 5.6% along transverse section and along longitudinal section, respectively. The tensile properties of ultimate tensile strength, yield strength and elongation were increased by 6.6%, 10.6% and 20.5%, respectively.

Declaration of Competing Interest

The authors declare that they have no known competing financial interests or personal relationships that could have appeared to influence the work reported in this paper.

Acknowledgements

This work was supported by the National Natural Science Foundation of China (No.52075022, No. 52074017), Beijing Natural Science Foundation (No. 3182020) and China-CEEC Joint Education Project for Higher Education (No. 2021113).

REFERENCES

[1] Wan Z, Zhao Y, Wang Q, Zhao T, Li Q, Shan J, et al. Microstructure-based modeling of the PMZ mechanical properties in 2219-T8 aluminum alloy TIG welding joint. Mater Des 2022;223:111133. https://doi.org/10.1016/j.matdes.2022.111133.
[2] Kuang X, Qi B, Zheng H. Effect of pulse mode and frequency on microstructure and properties of 2219 aluminum alloy by ultrahigh-frequency pulse Metal-Inert Gas Welding. J Mater Res Technol 2022;20:3391–407. https://doi.org/10.1016/j.jmrt.2022.08.094.
[3] Wang Y, Qi B, Cong B, Yang M, Liu F. Arc characteristics in double-pulsed VP-GTAW for aluminum alloy. J Mater Process Technol 2017;249:89–95. https://doi.org/10.1016/j.jmatprotec.2017.05.027. January.
[4] Lathabai S, Jarvis BL, Barton KJ. Keyhole gas tungsten arc welding of commercially pure zirconium. Sci Technol Weld Join 2008;13(6):573–81. https://doi.org/10.1179/136217108X329296.
[5] Vora JJ, Badheka VJ. Experimental investigation on mechanism and weld morphology of activated TIG welded bead-on-plate weldments of reduced activation ferritic/martensitic steel using oxide fluxes. J Manuf Process 2015;20:224–33. https://doi.org/10.1016/j.jmapro.2015.07.006.
[6] Pandya D, Badgujar A, Ghetiya N. A novel perception toward welding of stainless steel by activated TIG welding: a review. Mater Manuf Process 2021;36(8):877–903. https://doi.org/10.1080/10426914.2020.1854467.
[7] Huang Y, Fan D, Shao F. Alternative current flux zoned tungsten inert gas welding process for aluminium alloys. Sci Technol Weld Join 2012;17(2):122–7. https://doi.org/10.1179/1362171811Y.0000000087.
[8] Traidia A, Roger F. A computational investigation of different helium supplying methods for the improvement of GTA welding. J Mater Process Technol 2011;211(9):1553–62. https://doi.org/10.1016/j.jmatprotec.2011.04.008.
[9] Xiang J, Tanaka K, Chen FF, Shigeta M, Tanaka M, Murphy AB. Modelling and measurements of gas tungsten arc welding in argon–helium mixtures with metal vapour. Weld World 2021;65(4):767–83. https://doi.org/10.1007/s40194-020-01053-4.
[10] Lu S, Fujii H, Nogi K. Weld shape variation and electrode oxidation behavior under Ar-(Ar-CO2) double shielded GTA welding. J Mater Sci Technol 2010;26(2):170–6. https://doi.org/10.1016/S1005-0302(10)60028-X.
[11] Lu SP, Qin MP, Dong WC. Highly efficient TIG welding of Cr13Ni5Mo martensitic stainless steel. J Mater Process Technol 2013;213(2):229–37. https://doi.org/10.1016/j.jmatprotec.2012.09.025.
[12] Wang X. Finite volu pinchme simulation of arc:ing arc plasma by high-frequency alternating longitudinal magnetic field. 2022. https://doi.org/10.1063/5.0083796.
[13] Hu Y, Jiang R, Li X, Li A, Xie Z. Effects of high-intensity ultrasound on the microstructure and mechanical properties of 2195 aluminum ingots. Metals 2021;11(7). https://doi.org/10.3390/met11071050.
[14] Science P, Chen C, Zhang H. Understanding the changing mechanism of arc characteristics in ultrasound- magnetic field coaxial hybrid gas tungsten arc welding Understanding the changing mechanism of arc characteristics in ultrasound-magnetic field coaxial hybrid gas tungsten arc weld. 2022. https://doi.org/10.1088/2058-6272/ac7cb9.
[15] Wang Y, Chen M, Wu C. High-frequency pulse-modulated square wave AC TIG welding of AA6061-T6 aluminum alloy. Weld World 2020;64(10):1749–62. https://doi.org/10.1007/s40194-020-00953-9.

[16] Yang M, Li L, Qi B, Zheng H. Arc force and shapes with high-frequency pulsed-arc welding. Sci Technol Weld Join 2017;22(7):580–6. https://doi.org/10.1080/13621718.2016.1277625.
[17] Onuki J, Anazawa Y, Nihei M, Katou M, Onuma A, Funamoto T. Development of a new high-frequency, high-peak current power source for high constricted arc formation. Japanese J Appl Physics, Part 1 Regul Pap Short Notes Rev Pap. 2002;41(9):5821–6. https://doi.org/10.1143/jjap.41.5821.
[18] Cui SL, Liu ZM, Fang YX, Luo Z, Manladan SM, Yi S. Keyhole process in K-TIG welding on 4 mm thick 304 stainless steel. J Mater Process Technol 2017;243:217–28. https://doi.org/10.1016/j.jmatprotec.2016.12.027.
[19] Wang Y, Cong B, Qi B, Chen X, Yin Y, Lin S. Influence of low-pulsed frequency on arc profile and weld formation characteristics in double-pulsed VPTIG welding of aluminium alloys. J Manuf Process 2020;58:1211–20. https://doi.org/10.1016/j.jmapro.2020.09.025. August.
[20] Wang Y, Cong B, Qi B, Yang M, Lin S. Process characteristics and properties of AA2219 aluminum alloy welded by double pulsed VPTIG welding. J Mater Process Technol 2019;266:255–63. https://doi.org/10.1016/j.jmatprotec.2018.11.015. August 2018.
[21] Wang Y, Qi B, Cong B, Zhu M, Lin S. Keyhole welding of AA2219 aluminum alloy with double-pulsed variable polarity gas tungsten arc welding. J Manuf Process 2018;34(May:179–86. https://doi.org/10.1016/j.jmapro.2018.06.006.
[22] Sun X, Qi B, Jiang Z, Zeng C, Cong B. Refined weld microstructure and enhanced joint mechanical property of 1460 Al-Li alloys via double-pulsed variable polarity TIG arc welding. J Manuf Process 2022;82:738–49. https://doi.org/10.1016/j.jmapro.2022.08.044. August.
[23] Todaro CJ, Easton MA, Qiu D, Zhang D, Bermingham M, Lui E, et al. Grain structure control during metal 3D printing by high-intensity ultrasound. Nat Commun 2020;11(1):1–9. https://doi.org/10.1038/s41467-019-13874-z.
[24] Yang M, Yang Z, Qi B. Effect of fluid in molten pool on the welds with Ti-6Al-4V during pulsed arc welding. Int J Adv Manuf Technol 2015;81(5–8):1007–16. https://doi.org/10.1007/s00170-015-7272-2.
[25] Yuan T, Kou S, Luo Z. Grain refining by ultrasonic stirring of the weld pool. Acta Mater 2016;106:144–54. https://doi.org/10.1016/j.actamat.2016.01.016.
[26] Yuan T, Luo Z, Kou S. Mechanism of grain refining in AZ91 Mg welds by arc oscillation. Sci Technol Weld Join 2017;22(2):97–103. https://doi.org/10.1080/13621718.2016.1199127.
[27] Zhang D, Qiu D, Gibson MA, Zheng Y, Fraser H. StJohn D., et al. Additive manufacturing of ultrafine-grained high-strength titanium alloys. Nature 2019;576(7785):91–5. https://doi.org/10.1038/s41586-019-1783-1.
[28] Zeng C, Sun X, Qi B, Wang Y, Wang H, Tan Z, et al. In-situ TiC particles reinforced AA2219 Al-6.3Cu alloy joint via ultrasonic frequency double-pulsed arc. Mater Sci Eng A 2022;842(March):143078. https://doi.org/10.1016/j.msea.2022.143078.
[29] Wan Z, Wang Q, Zhao Y, Zhao T, Shan J, Meng D, et al. Improvement in tensile properties of 2219-T8 aluminum alloy TIG welding joint by PMZ local properties and stress distribution. Mater Sci Eng A 2022 Feb;839:142863. https://doi.org/10.1016/j.msea.2022.

Refining microstructure of medium-thick AA2219 aluminium alloy welded joint by ultrasonic frequency double-pulsed arc

Wang, Yipeng

2023-03-01

Wang Y, Li H, Li Z, et al., (2023) Refining microstructure of medium-thick AA2219 aluminium alloy welded joint by ultrasonic frequency double-pulsed arc. Journal of Materials Research and Technology, Volume 23, March-April 2023, pp. 3048-3061

https://doi.org/10.1016/j.jmrt.2023.01.174